Response of inelastic SDOF systems subjected to dynamic rupture simulations involving directivity and fling step

Karthik Reddy, K.S.K.; Somala, Surendra Nadh; Tsang, Hing-Ho

Published in:
Soil Dynamics and Earthquake Engineering

DOI:
10.1016/j.soildyn.2021.106992

Publication date:
2021

Response of Inelastic SDOF Systems Subjected to Dynamic Rupture Simulations involving Directivity and Fling Step

KSK Karthik Reddy[1,2*] Surendra Nadh Somala[1] Hing-Ho Tsang[2]

[1]Department of Civil Engineering, Indian Institute of Technology Hyderabad, India

[2]School of Engineering, Swinburne University of Technology, Melbourne, Australia

*corresponding mail id: surendra@iith.ac.in

This is the author accepted manuscript of the article: Karthik Reddy, KSK, Somala, SN & Tsang, H-H 2021, 'Response of inelastic SDOF systems subjected to dynamic rupture simulations involving directivity and fling step', Soil Dynamics and Earthquake Engineering, vol. 151, 106992. https://doi.org/10.1016/j.soildyn.2021.106992

Response of Inelastic SDOF Systems Subjected to Dynamic Rupture Simulations involving Directivity and Fling Step

Abstract

Directivity is a phenomenon perceived during fault ruptures wherein the ground motion and spectral response in the direction of the rupture is more significant than in any other direction. The objective of this study is to evaluate the variability in characteristics of near-fault ground motions as well as the ductility demand on structures due to directivity based on simulations of strike-slip earthquake events by employing SPECFEM3D, a physics-based ground motion simulation code. To understand the finite fault propagation effect, a source effect, the vertical strike-slip fault is considered to be embedded in an elastic half-space, to prevent the influence of path and site effects. Two scenarios are designed based on the positioning of nucleation asperity (NA): (1) in the middle of the fault face to simulate bilateral (BL) rupture and (2) shifted to one end for the case of unilateral (UL) rupture. The ground motions at near-fault stations, located in a racetrack configuration around the surface trace of the fault, are analyzed. In addition to a high spectral content in the forward directivity stations as a result of UL rupture, directivity velocity pulses identified in the fault-normal components are higher than the fling step velocity pulses in the fault-parallel component for the racetrack stations considered. Furthermore, the study examines the correlation between ductility demands computed based on elastoplastic rheology with Direct Point Parameter (DPP) and ground motion intensity measures for directivity and fling step stations.

Keywords: nucleation asperity, unilateral, bilateral, intensity measures, DDP, ductility demand

1 Introduction

Directivity definition has evolved with Somerville [1,2] from the late ’90s to mid-2000s from being the direction of slip aligning with the site of interest to rupture propagation towards it. Meanwhile, Abrahamson’s [3] definition of directivity uses a site away from the epicenter, still being close to the fault. Fling-step, which manifests in the fault parallel (FP) component in the case of vertical strike-slip faulting [4], should not be confused with directivity which is observed in the fault normal (FN) components of ground motion. Moreover, the velocity pulse is one-sided in the case of the fling step, while the two-sided pulse is observed in the case of directivity [3,5]. The one-sidedness and two-sidedness of velocity pulses in the near-fault can be understood from the fact that residual displacement is zero in the FN component, while there will be a permanent static offset in the FP component. So, the acceleration of the fling step can be represented by double impulse, while forward directivity requires triple impulse representation. In the case of the double impulse fling step acceleration, the polarities of the two pulses are equal and opposite. Triple impulse approximation of forward directivity acceleration has impulses separated by the same amount of time, with amplitudes of the first and third impulse taken as one-half of the middle impulse. So, the duration of the fling step and directivity pulses are also different. For inelastic systems, yielding can happen after the first impulse or the second impulse [6]. In the case of the triple impulse forward directivity pulse, note that the third impulse is smaller than the second impulse and so is unlikely to cause yielding, if yielding does not occur after the second impulse. Both directivity and fling step are near-fault effects, where the type of faulting and rupture propagation have a significant role to play apart from the magnitude of the earthquake.

Directivity is observed and reported in various earthquake events around the world. To start with a couple of examples, the 2003 Tehran Bam earthquake [7] and 1999 Chi-Chi earthquake (a thrust fault event) in Taiwan [8] depicts a dominance of the FN component and shift of peaks to a higher natural period in pseudo-spectral velocity. The distinct peak in spectral content is due to the presence of a pulse in the velocity time series. Moreover, the period of the pulse increases with an increase in the magnitude of the earthquake, and the increase in the period of the pulse causes the shift of peaks in spectral content towards higher natural periods [9]. Studies on the 2016 Meinong earthquake (Mw 6.18), also in Taiwan [10] used the classic method of finite fault inversion using data from a dense seismic array and concluded that directivity and site effects attributed from the mainshock caused devastating damage to the city of Tainan. Directivity was also observed during the Northridge earthquake at San Fernando Valley, California [11], where a station located up-dip displayed higher amplitudes than stations located in other orientations around the fault. A recent study on Ridgecrest Earthquake Sequence [12] also at California reported velocity pulse periods of the order 7.88 sec in the FN components extracted using Baker’s wavelet algorithm [13]. Polarization of spectral ordinates at periods close to that particular pulse period was highlighted by comparing the ratios of S_a (T_p)/$S_{aRotD100}$ (T_p) with pulse indicator (PI) [13,14]. Other directivity events include the 2011 Christchurch earthquake [15] in New Zealand and the Kobe earthquake in Japan [16] which resulted in catastrophic failure of buildings and infrastructure like the pipeline network damage. Further notable earthquakes in the Eurasian plate include the Lorca earthquake [17] in Spain and L'Aquila [18,19] in Italy. The characteristics of recent strong ground motion recordings of earthquake sequence (2016-2017) in Italy [20] collected using a dense network of

seismographs featured forward directivity and fling effects. A comparison with the existing Bindi's GMPE [21] showed that the source directivity effects were underestimated in this region.

The pulse periods and amplitudes vary among stations depending on their locations with respect to the fault and source characteristics [22], such as friction coefficient, stress drop, distribution of slip, and fault styling. Though these effects have also been reported for smaller magnitude earthquakes [23], the reasoning behind the lack of directivity in events of magnitude smaller than 5 can be attributed to the dimensions of the fault relative to the rupture velocity. The relation between the magnitude of an earthquake and its fault dimensions is well described in the work by Leonard [24], which suggests that earthquakes of magnitude 7 or 8 require the rupture to propagate over a large area (and so longer lengths), resulting in higher amplitudes in the direction of rupture as reflected in the velocity time series.

Somerville et al. [25] recommended the first set of empirical relations to account for the spectral amplification due to directivity. However, even after the application of the empirical relations, the peak spectral amplitudes recorded during the historic earthquakes (1995 Kobe, 1994 Landers, and 1989 Loma Prieta earthquake) are 50% larger than the average horizontal components using this model [25] predicted for a magnitude 7 event at a station located 5 km from the fault line [26]. Later an augment to this model [25] to contain duration and amplitude effects was proposed [1]. A final improved version of Somerville et al. [1] dealing with the unnormalized fault length is suggested in the NGA West-2 report [27]. This model is based on variables that determine the failure mechanism of the fault, fraction of fault length ruptured with respect to the position and orientation of the site and the epicenter. The Uniform Building Code (UBC) [28] has considered this directivity amplification effect based on the source-to-site distance which is limited to sites located less than 15 km from the fault as observed by Akkar et al. [29,30].

With a better understanding of the directivity effect, it is desirable to take this into account in probabilistic seismic hazard analysis (PSHA). Chioccarell et al. [31,32] found that the incorporation of directivity effects into PSHA tends to increase the ground motion intensity by more than 100% at a particular return period depending on the site locations with respect to the fault plane. Similar studies by Shahi et al. [14] found that the ground motion intensities are higher at the ends of the fault for bilateral (BL) ruptures. Such contours showcase the consideration of directivity within the PSHA framework.

A fling step is better perceived in the displacement time series which can be split into zero amplitude till the arrival time (t_a) and duration of permanent offset (T_p) corresponding to displacement amplitude (D_p) [33]. The 1999 Chi-Chi earthquake (Mw =7.6) reported a maximum (D_p) of 652 cm [33,34]. Several other earthquakes include the 1999 Kocaeli (Mw =7.6), 2010 Darfield (Mw =7), and El Mayor-Cucapah (Mw =7.2) which reported a range of D_p between 17.9 cm to 176 cm [33,34]. The correlation between displacement pulse (T_p) and earthquake magnitude is similar to the correlation between magnitude and near-fault fling parameters [35,36] and velocity pulse [14,37] .

Nevertheless, there is a paucity of research on the spatial variability in characteristics of near-fault ground motions produced by changes in source characteristics accounting for directivity.

Particularly, numerical simulations using rupture dynamics can provide complete time series for both FP and FN components of ground motion at locations equidistant to the fault (same R_{rup}), for all azimuths, thereby facilitating detailed quantification of changes in the cyclic response of structures in close proximity to the fault. In this article, we address this complex issue by simulating UL-rupture and BL-rupture of equal magnitude and demonstrate the azimuthal variability of ground motions characteristics as well as the ductility demand put on structures by these ground motions.

The rest of the paper is organized as follows: the literature on the behavior of structures excited at the base by FP and FN velocity pulses, followed by the description of dynamic rupture earthquake simulations along with the material properties and stresses and friction used to compute FP and FN ground motion, the characteristics (PGV, pulse period, spectral content) of the simulated ground motion. The simulated ground motion is used to evaluate the ductility demand of elastoplastic SDOF systems with varying natural periods for FP and FN components separately and the interrelationship between the ductility demand and ground motion characteristics is presented along with the directivity parameters.

2 Response of structures subjected to directivity and fling-step velocity pulses

Ground motion classification as near-fault ground motion is based on hypocentral depth and Joyner–Boore distance (R_{jb}), while the hypocentral depth is limited to 40 km, the R_{jb} can extend upto 140 km as given in a study by Pocar et al. [38].

A simplified representation of forward directivity (FN) and fling step (FP) velocity pulses was proposed by Hall et al. [39] as well as Kalkan and Kunnath et al. [5]**.** The former classified pulse-like ground motions into forward (consisting of only half-wave signal) and forward and back motion (consisting of full-wave signal) and concluded that ground motions comprising of full-wave signal resulted in severe damage to structures, the latter used steel structures of varying natural periods and deduced that fling-step ground motions will generate a higher inter-storey drift for lower stories and forward directivity ground motions result in a higher inter-storey drift for moderate and high stories. Moreover, structures exhibited the highest Interstory Drift Ratio (IDR) when the ratio of T_p/T approaches unity in the case of fling step pulse, while for forward directivity ground motions highest (IDR) was observed when the ratio (T_p/T) is lower than 1. Kalkan and Kunnath [5] also quoted the fact that the fling step results in maximum demand as a function of fundamental frequency while the forward directivity effect causes higher models to activate.

Inelastic analysis of the SDOF system with varying fundamental period and reduction factors using the Modified Takeda model showed that isolating the fling step effect from ground motions resulted in higher seismic demand in structures [40]. Studies on the response of tall structures to fling step include analysis by Ventura et al. [41] where inclusion of fling displacement in ground motion significantly increased the seismic demand of tall structures. Structural response to forward-directivity ground motions as a function of pulse periods has also been investigated by Sehhati et al. [42]. The period of the velocity pulses extracted by using Gabor wavelet functions [13] was used to compute the ductility demand of 3, 7, and 14-story [42]. In their study, it is reported that pulse-like forward directivity ground motions imposed a greater ductility demand in

structures. Studies on the influence of pulse period ground motions on buildings by Champion et al. [43] show that the probability of damage in a modern concrete structure is 6% to near field pulse-like ground motions while it is 1% in the case of far-field ground motions. Madina et al. [44] studied the influence of various bilinear hysteresis models on the engineering demand parameters of structures with natural periods ranging from 0.3 to 3.6 sec and found a non-uniform distribution of peak drifts along the height of the structure. Furthermore, the necessity of benchmarking the seismic response of a Single Degree of Freedom (SDoF) to evaluate the response of complex Multidegree of Freedom System (MDoF) structures has been emphasized. In this study, the structures are idealized as elastoplastic SDoF models, the details of which can be found in the later sections.

3 Dynamic Rupture Simulations

Physics-based numerical approaches represent an emerging tool for earthquake ground motion prediction (especially within 20 km distance, where there is paucity in strong motion recordings) making empirical predictions less constrained. To capture directivity in simulated ground motion, one cannot rely on stochastic simulation methods (EXSIM [45] and SMSIM [46,47]) that modulate Gaussian white noise with an envelope function. Such stochastic approaches do not fully capture the physics of the seismic source [48]. Kinematic as well as dynamic earthquake ruptures both require 3D numerical implementation of elastodynamic equations, coupled with ways to update the displacement evolution of the fault nodes. In this work, we use a 3D spectral element method [49], a higher-order finite element approach with 5 Gauss-Lobatto-Legendre (GLL) integration points, by which ground motions can either be computed based on kinematic or dynamic approaches.

The numerical method for elastodynamic equations in the form of the finite-difference method was first introduced by Smith [50] into seismology. These methods were also used to simulate the propagation of waves in stratified media and sedimentary basins to assess ground-motion amplification [51]. The initial 3D simulations were performed by Frankel et al. [52], who simulated and validated a magnitude 4.4 aftershock of the 1989 Loma Prieta, California, earthquake using a point source model. With the recent advances of the computational facility, rigorous models were created and simulated across the range of spectral frequencies of engineering interest [53,54]. Kinematic approaches [55,56] prescribe arbitrary (i) slip, (ii) rise time, and (iii) rupture time (or rupture velocity), without any basis to the physics behind how such a spatio-temporal evolution of slip is possible. The simplest of the source time functions for slip is a ramp function whose onset is at rupture time, and saturation occurs within rise time from the onset. The ramp in slip is a pulse in slip rate (also known as slip velocity). Such a source time function is scaled by the amount of slip. Dynamic rupture simulations, on the other hand, depend on the stresses (or forces) and are based on fracture mechanics principles. Only initial conditions (stresses) are prescribed, unlike in kinematic approaches where the entire temporal evolution is pre-defined, and the rupture is let to propagate spontaneously based on contact-friction laws. A detailed discussion on dynamic rupture compatible source time functions for kinematic rupture is presented in Tinti et al. [57]. One of the biggest advantages of physics-based simulations is the possibility to get ground motion waveforms, rather than just the peak values. However, it should

be noted here that except for very idealized cases - as the one considered here - the generation of broadband ground motion is a challenge in physics-based numerical simulations.

Shear fractures

Earthquakes are modeled as mixed-mode (mode II & mode III) shear fractures on the fault plane whose propagation is governed by contact-friction laws. Contact conditions prevent interpenetration of the two sides of the fault. The ratio of shear to normal traction has an upper bound, which is the friction coefficient. Slip (relative displacement across the two sides of the fault) occurs when the background shear traction exceeds the friction at a given location and at a particular time. Either the slip velocity should be zero or the ratio of shear to normal is precisely equal to the friction coefficient. In addition, the resultant slip velocity is considered to point in the same direction as the resultant shear traction in mixed mode rupture propagation.

Friction, typically used, weakens linearly with slip [58–60] from static (μ_s) to dynamic level ($\mu_d < \mu_s$) as slip increases from zero to a length-scale parameter known as slip-weakening distance (D_c), as shown in Figure 1. However, other kinds of weakening (say, nonlinear), and other weakening mechanisms (say, with respect to time), also exist in literature. More advanced friction laws incorporate rate (slip velocity) dependency of friction evolution, along with state variables [61,62].

Three different shear stress levels correspond to three of the friction coefficients. The three levels are static (μ_s), dynamic (μ_d), and initial ($\mu_0 < \mu_s$). At each of these levels, shear stress is the product of normal stress (σ) and the corresponding friction coefficient. So, static stress (τ_s) equals $\mu_s\sigma$and dynamic stress (τ_d) equals $\mu_d\sigma$, both acting in the direction opposite to the direction of the rupture propagation. The initial friction coefficient (μ_0), which is the ratio of the initial shear stress ($\tau_0 < \tau_s$) to the initial normal stress (σ_0), on the fault plane. On a small portion (nucleation size) of the fault, shear stress is perturbed slightly beyond the static level ($\tau_{nuc} > \tau_s$) so that rupture initiates. Once initiated, the rupture propagates spontaneously until it hits a barrier (very high friction), which is placed beyond the boundaries of the rupture dimensions. The nucleation size must be sufficiently large [63], otherwise, the rupture dies out much earlier without propagating till the barrier. Energy-based approaches, on the other hand, require the energy release rate to be greater than the energy absorbed by the fracture growth, for the rupture to continue propagating spontaneously. The fracture energy (G_c) can be computed from Figure 1 as the area of the right-angled triangle whose one of the sides is the difference between static and dynamic friction coefficient and the other side is the slip-weakening distance [64]. One critical aspect of dynamic rupture simulations is the grid spacing should be fine enough to resolve the cohesive zone (or slip weakening zone) behind the rupture tip, as it undergoes Lorentz contraction in the rupture propagation direction [65].

Modeling and Meshing

To focus on the source effect of directivity, a flat top model is chosen with a homogeneous velocity model. In particular, we use a model motivated by SCEC dynamic rupture code validation group's TPV3 [66,67]. A slightly modified version is used, whose parameters are mentioned in Table 1. The vertical strike-slip fault in the middle of the domain reaches the free surface. The

young's and shear moduli of the medium are defined in terms of primary (P) and secondary (S) wave velocities. For the elastic isotropic medium, apart from lame's constants, density is required to complete the description of the medium. A Poissonian solid ($\nu = 0.25$) is used. Meshing is done in such a way that the size of the mesh is fine enough to resolve for the frequency range of interest. The lower the wave speeds in the medium, the finer the mesh needs to be for a particular resolving frequency in the model. The dynamic rupture simulations need high-performance computing (HPC) to calculate ground motion within a reasonable amount of time.

An idealized two-dimensional vertical strike-slip fault, analogous with the San Andreas fault in Southern California, is modeled in an elastic half-space, as shown in Figure 2(a) [66]. The domain covers 60 km x 60 km in map view. The fault plane lies on the XZ plane. Figure 2(a) shows the geometry of the fault plane and earth domain considered for simulations. Rupture propagation on the fault is restricted to an area of 30 km x 15 km as shown in Figure 2(b). The depth of the fault is chosen based on the seismogenic depth of the San Andreas fault in Southern California, and the length is fixed based on scaling laws for the magnitude of interest (M_w 7). Rupture is initiated in a 3 km x 3 km patch (asperity) by artificially perturbing the initial stress to frictional failure. The extended fault plane is shown in Figure 2(b). Bi-lateral (BL) rupture is denoted by a blue cross where rupture initiation is in the middle of the fault, while uni-lateral (UL) rupture is denoted by a yellow cross, where rupture initiates at one end of the fault.

Both the simulations are done by using identical dimensions and orientations of the fault plane and earth domain. The material properties, stresses, and frictional parameters used for both the simulations are shown in Table 1. The positions of the five stations are aligned around the fault in a racetrack fashion at a distance of 10 km from the fault as shown in Figure 2(c). To understand the directivity effects, for both scenarios, station 1 is considered. One can rely on station 3 to understand the backward directivity effect. Station 2 can be treated as a fling step station for the BL-rupture scenario. Similarly, the S4 station is considered as a fling step station for the UL-rupture scenario. The location of stations shown is adapted from Dabaghi et al. [68] whose work is presented at the 5th International Symposium on the Effects of Surface Geology (ESG5). Figure 3 shows the evolution of slip rate for BL (left column) and UL (right column scenario ruptures) scenarios. In the case of BL rupture, the rupture front reached the ends of the fault in 4-5 sec, while in UL rupture the rupture front took in excess of 9 sec to reach the fault tip closest towards the forward-directivity station (S1). Figure 4 shows the final slip distribution on the fault plane. Rupture time contours are also superimposed on top of the slip distribution in Figure 4. As expected, the BL rupture took the same amount of time to reach the forward-directivity (S1) as well as backward-directivity (S3) stations. In the case of the UL rupture, however, the rupture reached the fault tip towards the backward-directivity (S3) station in just 1 sec, while it took more than 9 sec to reach the forward-directivity (S1) fault tip.

4 Elastic and Inelastic SDOF Systems

In this study, the response of structures idealized as elastoplastic systems is shown in Figure 5 along with the corresponding linear system. The elastoplastic or the ideal bilinear model can be

defined based on the stiffness of the structure (k_1) until a yield displacement of (u_y) corresponds to the yield force (f_y). The yield force (f_y) is typically considered as the desired percentage of (f_0) which is the minimum strength required by the SDoF system to remain linearly elastic during the ground motions. Beyond yield displacement (u_y), the structure progresses into a plastic regime where stiffness (k_2) initializes until the maximum deformation (u_m) is attained. The ratio of (f_y/f_0) or (u_y/u_0) is defined as the normalized yield strength ($\underline{f}_y$). Alternatively, yield strength reduction factor R_y (written interchangeably as R, dropping the subscript 'y', in this work) which is inverse of ($\underline{f}_y$) can also be used to represent the correlation. A value of R_y 1 represents $f_y = f_0$, while R_y 2 represents that the yield force (f_y) is one-half of the required force (f_0). R_y 1,3 & 5 are considered in this study.

5 Results and Discussion

The Peak ground velocity (PGV) contours over the domain are depicted in Figure 6. It is to be noted that for strike-slip faults, PGV from the FN component prevails parallel to the strike and the FP component prevails perpendicular to the strike. On comparing the PGVs from BL rupture (Figure 6a) and UL rupture (Figure 6b), it can be seen that the PGV in the regime of forward directivity stations is higher in the case of UL rupture. The fraction of the fault rupture in between the hypocentre and the forward directivity stations is an influential parameter in governing the PGV amplitude for FN components. The fling step pulse is observable in the FP components. Stations susceptible to the fling step are located along the line passing through NA and perpendicular to the strike.

Pulse Periods of the Race Track Stations

Figure 7 shows the comparison of velocity-time series in FP and FN directions for the UL and BL-rupture scenarios. The ground motions recorded at stations on a racetrack equidistant (same R_{rup}) from the fault are further classified as pulse-like or non-pulse type, using the wavelet pulse classification algorithm of Baker and co-workers [13,14]. It is to be noted here that Baker's algorithm has lower than 30 cm/s peak velocity as a threshold for the rejection of the presence of a pulse. In this study, the generated ground motions for the magnitude 7 earthquake contain a pulse in specific components and at particular stations. In the BL-rupture scenario, pulse periods of 1.78 sec were identified in the FN components at S1 as well as S3 as shown in (Figure 8), no pulse was identified in the FP components. Note that bilateral ruptures also have a propagation length effect that is about half that of the forward directivity station of the UL-rupture scenario. The difference between forward and backward is imperceivable as the length of propagation to each of these stations is the same in the case of the BL-rupture scenario.

In the UL-rupture scenario, a slightly higher pulse period (2.36 sec) (Figure 8) is identified in the FN component of forward directivity station (S1) and a pulse period of 1.43 sec is observed in the backward directivity station (S3). The magnitude-pulse empirical scaling model proposed by Chioccarelli et al. [69] reported a median Tp value of 3.65 sec for a 7 magnitude earthquake, while the inclusion of one positive standard deviation reported a Tp value of 6.58 sec. Ground

motions from the mainshock of Ridgecrest earthquake sequence [12] also reported pulses of the order 7.868 sec and 8.477 sec at stations WRV2 and WMF, respectively. Pulse periods (1.33 sec & 1.14 sec) were also identified in the FP component at fling step stations S2 and S4 for BL and UL ruptures, respectively.

Fourier Amplitude Spectra

Figure 9 shows the Fourier amplitudes of acceleration at the 5 stations. The fourier amplitudes of the FN component of forward-directivity stations is clearly higher than those of backward-directivity stations irrespective of the corner frequencies. A study on the directivity of small earthquakes in the Abruzzo region, Italy [70] showed diminishing spectral amplitudes at higher frequency content in backward stations when compared to forward directivity stations. It is also possible to quantify the change in corner frequency as a result of the shift in NA using the directivity coefficient (C_d) given by Ben-Menahem [71].

Constructive interference pattern leads to a high single corner frequency, a single drop-down kink is observed in acceleration amplitudes of forward directivity stations. Anti directivity or backward directivity stations exhibit multiple kinks as a result of S-waves reaching the station in time intervals. Such multiple kinks are also observed in FP components.

Response Spectra

Figure 10 shows a comparison of the acceleration response spectra for the FP and FN components for both the rupture scenario cases. Station 1 has a higher spectral acceleration in FN components. When comparing UL-rupture to BL-rupture, there is dominance in spectral acceleration for FN components well beyond the natural period of 1 sec. Such factors can be integrated into a BL response spectrum to account for maximum directivity effects. Similar post factors were suggested by Somerville in the NGA West-2 report [27] to reconstruct existing response spectra with directivity effects. At Station 2, a higher FP component is evident in the velocity time series (Figure 7) which is reflected in the spectral content (Figure 10) as well. The higher FP component over the FN component is due to station 2's proximity to the NA in the bilateral rupture event.

For the case of UL rupture, S3 is a backward directivity station and S4 is a fling step station. At S3, a comparison of UL (FN) and BL (FN) reveals a decrease in spectral content for the backward directivity station at all natural periods. When compared to the FP component of BL rupture. The fling phase in UL rupture being persistent in the FP component dominates the spectral acceleration at S4. The comparison of FP and FN response spectra at station 5 demonstrates that the UL (FP) spectrum is higher than BL (FP). Similarly, the UL (FN) spectrum is higher than BL (FN).

Constant Strength Reduction Factor Response Spectra

Existing seismic design requirements typically allow the structure to advance into an inelastic state when subjected to strong ground motions. Studies [72–74] have shown a close relation exists between the damage characteristic of a structure and the ductility factor. Factors influencing the ground motion characteristics like soft soil and near field [74] reported a higher

ductility demand than those obtained using the smooth design response spectra (IBC 2000) [75]. Other factors include intensity measure factors like duration ($D_{s5\text{-}75}$) [76] which showed that long-duration ground motions impose a higher ductility demand than short-duration ones. Studies have reported that the ductility demand of the structure is highly influenced by source site distance [77,78].

Figure 11 shows the comparison of ductility demand spectra the FP and FN components in both rupture cases for yield strength reduction factor R_y 1,3 & 5. The FN component of forward directivity station S1 exhibits a higher ductility demand in the acceleration and partial velocity-sensitive regions (until 1 sec) for the UL rupture scenario than the BL rupture scenario. While a reversal in the trend of ductility factors (lower ductility factors in the acceleration and velocity region at S3-UL) was observed on comparing both the rupture scenarios in the backward directivity regime. At fling step stations S2, higher ductility demand was observed for UL (FP) components in the acceleration and velocity-sensitive regions despite higher spectral content of the FP-component of BL over the FP-component of UL. This conflicting pattern in ductility requirement may be due to the fact that ductility factors are computed for constant strength reduction factors rather than for a constant yield strength. Similarly, S4 which is a fling step station for the UL rupture scenario also exhibited lower ductility demand when compared to the S4 of BL rupture. But in the displacement sensitive regime, a reverse trend is observed. At S5 station, there is insufficient distinguishability when comparing ductility demands from components of both scenario ruptures.

Bayless and Somerville (2013) Correction Factors for Directivity

The geometric directivity predictor expressed as $ln(s)[1 + cos(2\theta)]/2$expressed in terms of unnormalized lengths is used as a correction for directivity in the NGA West-2 model of Bayless and Somerville (2013) (BS2013) [79] which is a modified ground motion prediction model of Somerville et al. 1997 [1]. This factor is computed for bilateral and unilateral ruptures and is shown in Figure 12. The ductility demands of structures with natural periods of 0.3 sec, 1 sec, and 3 sec at Ry 5 are superimposed over the BS2013 correction factors in Figure 12.

The pattern in the ductility demand of the SDoF system with a natural period of 0.3 sec was identical to Bayless and Somerville's directivity predictor at the relevant stations when subjected to FN component ground motions from both scenario ruptures. The BS2013 directivity metric had little or no link with the ductility demand requirements of SDoF systems with natural periods of 1 sec and 3 sec.

Chiou and Spudich (2013) DPP

The Isochrone Directivity Parameter (IDP) given by Spudich and Chiou (2008) [80] is based on the projected point from the station onto the fault plane. In 2013, the same authors formulated DPP with respect to the "direct point" expressed in terms of a different isochrone velocity ratio $\hat{c}$' [27] (CS2013). The rupture velocity in our case (Figure 4) is slightly higher than 0.8 times the shear-wave velocity. The correlations of ductility demand with respect to DPP are shown in Figures 13, for the two horizontal components of bilateral and unilateral ruptures. The

relationship between ductility demands of inelastic SDoF systems and DDP parameters is similar to Bayless and Somerville's directivity parameter.

Intensity Measures (IMs)

The correlations between various ground motion intensity measures (IMs) and the peak as well residual hysteretic displacements are shown in Figures 14. The IMs considered here are Peak Ground Acceleration (PGA [g]), Peak Ground Velocity (PGV [m/s]), Peak Ground Displacement (PGD [m]), PGA to PGV ratio (Hz) [81], Root Mean Square of acceleration (RMS_acc [g]) [82], Root Mean Square of velocity (RMS_vel [m/s]) [83] , Root Mean Square of displacement (RMS_dis [m]), Arias Intensity (Ia) [84], Characteristic Intensity (Ic), Specific Energy Density (SED), Cumulative Absolute Velocity (CAV) [85], Acceleration Spectrum Intensity (ASI) [86], Velocity Spectrum Intensity (VSI) [86] and Housner Intensity (HI) [87]. The intensity measures are evaluated at the 5 racetrack stations and the ductility demands at Ry 5 are superimposed for the 3 (0.3 sec,1 sec, and 3 sec) natural periods.

It is indeed difficult to identify a consistent relationship between a specific ground motion measurement and the SDoF system's ductility demand. However, the most closely overlapping patterns of ground motion intensities with the ductility demand have been emphasised. PGA and PGV showed better correlation with ductility demands for natural periods 3 sec and 0.3 sec for BL (FP) (except for S2) and BL (FN) (except for S5) components. Intensity measures like RMS_acc, RMS_vel and RMS_disp exhibited correlation similar to PGA,PGV and PGD with the ductility factors. Ia and Ic intensity measures of BL-rupture are more suitable in assessing the ductility demand for 3 sec natural period structures than UL-rupture. The best correlation is found between intensity measure SED and ductility demands at natural periods (0.3-1 sec) for both the components of both the ruptures. The correlation pattern reported with ASI, VSI, and HI intensity measures are identical, with the exception that the scales are different. It is advised to rely on various ground motion intensities depending on the station location as well as the kind of rupture scenario. For instance, except for the BL (FN) component, PGD also exhibited one of such patterns for natural periods of 0.3-1 sec with an exception at station S2-BL (FP).

7 Conclusions

Earthquakes simulated using physics-based dynamic ruptures can be used to capture the spatial variability of velocity pulses in both FN (directivity) and FP (fling step) components of near-fault ground motions. By shifting the NA from the center of the fault to one of the sides, a bilateral rupture analogous to SCEC dynamic rupture benchmark TPV3 (San Andreas faulting mechanism with comparable seismogenic depth) is converted into a unilateral rupture. The characteristics of ground motions for the unilateral and bilateral cases differ based on the orientation of stations on a racetrack surrounding the surface trace of the fault. Forward and backward directivity stations of unilateral rupture show velocity pulses in the FN component, as expected. Fling step pulse is observed in the FP component at a couple of stations that lie close to

the axis perpendicular to the fault passing through the epicenter, of which the bilateral case is dominant at station S2, while the unilateral case is dominant at station S4.

The conclusions are split into 2 categories: (i) Influence of source on near-source ground motion characteristics where the spectra of the time series in conjunction with pulse periods were reported, (ii) Impact of near-source intensity features on inelastic structural response.

Influence of source on near-source ground motion characteristics

- As the position of NA is changed from BL rupture to UL rupture, the PGV distribution becomes asymmetrical, with larger PGVs biased towards forward directivity stations when compared to the identical station PGV from BL rupture. While the proportion of fault ruptured between the hypocentre and site determines the PGV of forward directivity stations, the position of fling step stations is determined purely by the location of NA, regardless of the fault rupture length.

- An increase and decrease in pulse periods are observed in forward directivity station S1 UL (FN) and backward directivity station S3 respectively as a result of the change in NA. Pulse periods reported at the fling step stations were lower than those reported at the forward directivity stations of BL rupture.

- Higher spectral amplitudes were observed in the forward directivity station ground motions of UL rupture when compared to the same ground motions at the same station from BL rupture. While at the backward directivity station, a reversal of trend is observed.

- The FP component of fling step stations (S2 for BL and S4 for UL) have higher spectral acceleration than their counterparts. The rise or drop of kinks in the Fourier acceleration amplitudes at these stations is a result of differences in seismic wave arrivals from the rupture sequence on the fault plane.

Impact of near-source intensity features on inelastic structural response

- Though higher ductility demands were found at forward directivity stations for a natural period of 0.3 sec, fling step stations also reported high ductility demands for all the 3 considered natural periods (0.3 sec, 1 sec, and 3 sec).

- BS2013 [79] and CS2013 [28] directivity parameters based on station's position relative to hypocentre correlate well with the ductility demand at natural periods of 0.3 sec derived for FN components of the respective station's ground motions.

- The ductility demand calculated for natural periods (0.3-1sec) correlates better with the intensity measures PGD, RMS disp, and SED. Ductility factors for a natural period of 3 sec correlate better with PGA and PGV.

Halfspace model and bedrock level (Vs = 3.46 km/s) synthetic ground motions are deliberately considered to isolate other effects like local site conditions (with Vs30 of the order of a few hundreds of m/s) and path effects (layered velocity model). Even the nucleation asperity is kept close to the free surface, to eliminate mode III (dip-slip) propagation effects from deeper hypocenters. Future works can potentially focus on combining source effects like directivity and fling step coupled with site effects. Typical 3D earthquake simulations restrict themselves to frequencies lower than 1 Hz, owing to the limited knowledge of the detailed 3D velocity model of a region. Higher frequencies are either coupled stochastically [88] or using artificial neural networks [89] to combine with low-frequency deterministic simulations to obtain broadband ground motion of interest to engineers. Using rough faults, dynamic rupture simulations are helping in the deterministic computation of higher frequencies [90]. Moreover, for every doubling in frequency of resolution in 3D simulations, the computational cost goes up 2^4 = 16. Furthermore, the shallow layers with a few hundreds of m/s shear wave velocity can mandate finer mesh, which in turn lowers that stable timestep. The present study can be easily extended to other magnitudes and dipping fault configurations. Moreover, multiple simulations can be conducted exploring the variability of the input parameters to quantify the range of hysteresis response.

Acknowledgments

The authors thank the two anonymous reviewers, whose comments and suggestions have significantly improved the manuscript. This study is partly funded by the Ministry of Earth Sciences (MoES), India under the grant number MoES/P.O.(Seismo)/1(304)/2016.

References

[1] Somerville PG, Smith NF, Graves RW, Abrahamson NA. Modification of Empirical Strong Ground Motion Attenuation Relations to Include the Amplitude and Duration Effects of Rupture Directivity. Seismological Research Letters 1997;68:199–222. https://doi.org/10.1785/gssrl.68.1.199.

[2] Somerville PG. Engineering characterization of near fault ground motions. Proceeding of the SMIP97 seminar, Citeseer; 2005, p. 9–28.

[3] Abrahamson N. Incorporating effects of near fault tectonic deformation into design ground motions, a presentation sponsored by the Earthquake Engineering Research Institute Visiting Professional Program, hosted by the University at Buffalo, 26 October 2001. 2001.

[4] Hisada Y, Tanaka S. What Is Fling Step? Its Theory, Simulation Method, and Applications to Strong Ground Motion near Surface Fault Ruptures. Bulletin of the Seismological Society of America 2021.

[5] Kalkan E, Kunnath SK. Effects of fling step and forward directivity on seismic response of buildings. Earthquake Spectra 2006;22:367–90.

[6] Kojima K, Saotome Y, Takewaki I. Critical earthquake response of a SDOF elastic-perfectly plastic model

with viscous damping under double impulse as a substitute for near-fault ground motion. Japan Architectural Review 2018;1:207–20.
[7] Yaghmaei-Sabegh S, Tsang HH. An updated study on near-fault ground motions of the 1978 Tabas, Iran, earthquake (Mw= 7.4). Scientia Iranica 2011;18:895–905. https://doi.org/10.1016/j.scient.2011.07.018.
[8] Phung V, Atkinson GM, Lau DT. Characterization of directivity effects observed during 1999 Chi-Chi, Taiwan earthquake. 13th World Conference on Earthquake Engineering, Vancouver, BC, Canada, August, 2004, p. 1–6.
[9] Somerville PG. Magnitude scaling of the near fault rupture directivity pulse. Physics of the Earth and Planetary Interiors 2003;137:201–12. https://doi.org/10.1016/S0031-9201(03)00015-3.
[10] Lin Y-Y, Yeh T-Y, Ma K-F, Song T-RA, Lee S-J, Huang B-S, et al. Source characteristics of the 2016 Meinong (ML 6.6), Taiwan, earthquake, revealed from dense seismic arrays: Double sources and pulse-like velocity ground motion. Bulletin of the Seismological Society of America 2018;108:188–99.
[11] Wald DJ, Heaton TH, Hudnut KW. The slip history of the 1994 Northridge, California, earthquake determined from strong-motion, teleseismic, GPS, and leveling data. Bulletin of the Seismological Society of America 1996;86:S49–70.
[12] Baltzopoulos G, Luzi L, Iervolino I. Analysis of Near-Source Ground Motion from the 2019 Ridgecrest Earthquake Sequence. Bulletin of the Seismological Society of America 2020;110:1495–505.
[13] Baker JW. Quantitative classification of near-fault ground motions using wavelet analysis. Bulletin of the Seismological Society of America 2007;97:1486–501.
[14] Shahi SK, Baker JW. An Empirically Calibrated Framework for Including the Effects of Near-Fault Directivity in Probabilistic Seismic Hazard AnalysisFramework for the Effects of Near-Fault Directivity in Probabilistic Seismic Hazard Analysis. Bulletin of the Seismological Society of America 2011;101:742–55. https://doi.org/10.1785/0120100090.
[15] Bradley BA, Baker JW. Ground motion directionality in the 2010-2011 Canterbury earthquakes. Earthquake Engng Struct Dyn 2015;44:371–84. https://doi.org/10.1002/eqe.2474.
[16] Takada S, Hassani N, Fukuda K. Damage directivity in buried pipelines of Kobe city during the 1995 earthquake. Journal of Earthquake Engineering 2002;6:1–15.
[17] Gordo-Monsó C, Miranda E. Significance of directivity effects during the 2011 Lorca earthquake in Spain. Bulletin of Earthquake Engineering 2018;16:2711–28.
[18] Calderoni G, Rovelli A, Ben-Zion Y, Di Giovambattista R. Along-strike rupture directivity of earthquakes of the 2009 L'Aquila, central Italy, seismic sequence. Geophysical Journal International 2015;203:399–415.
[19] Calderoni G, Rovelli A, Di Giovambattista R. Rupture directivity of the strongest 2016–2017 central Italy earthquakes. Journal of Geophysical Research: Solid Earth 2017;122:9118–31.
[20] Luzi L, Pacor F, Puglia R, Lanzano G, Felicetta C, D'Amico M, et al. The central Italy seismic sequence between August and December 2016: Analysis of strong-motion observations. Seismological Research Letters 2017;88:1219–31.
[21] Bindi D, Massa M, Luzi L, Ameri G, Pacor F, Puglia R, et al. Pan-European ground-motion prediction equations for the average horizontal component of PGA, PGV, and 5%-damped PSA at spectral periods up to 3.0 s using the RESORCE dataset. Bulletin of Earthquake Engineering 2014;12:391–430.
[22] Rezaeian S, Der Kiureghian A. Simulation of synthetic ground motions for specified earthquake and site characteristics. Earthquake Engineering & Structural Dynamics 2010;39:1155–80.
[23] Boatwright J. The persistence of directivity in small earthquakes. Bulletin of the Seismological Society of America 2007;97:1850–61.
[24] Leonard M. Earthquake Fault Scaling: Self-Consistent Relating of Rupture Length, Width, Average Displacement, and Moment Release. Bulletin of the Seismological Society of America 2010;100:1971–88. https://doi.org/10.1785/0120090189.
[25] Somerville PG, Smith NF, Graves RW, Abrahamson NA. Representation of near-fault rupture directivity effects in design ground motions, and application to Caltrans bridges. Proceedings of the National Seismic Conference on Bridges and Highways, 1995, p. 10–3.
[26] Somerville PG, Smith NF, Graves RW, Abrahamson NA. Accounting for near-fault rupture directivity effects in the development of design ground motions. ASME-PUBLICATIONS-PVP 1995;319:67–82.
[27] Spudich P, Bayless JR, Baker JW, Chiou BS, Rowshandel B, Shahi SK, et al. Final report of the NGA-West2 directivity working group 2013.
[28] Officials IC of B. Uniform building code. vol. 2. International Code Council; 1997.
[29] Akkar S, Moghimi S. Implementation of Near-Fault Forward Directivity Effects in Seismic Design Codes. European Conference on Earthquake Engineering Thessaloniki, Greece, Springer; 2018, p. 183–201.

[30] Akkar S, Moghimi S, Arıcı Y. A study on major seismological and fault-site parameters affecting near-fault directivity ground-motion demands for strike-slip faulting for their possible inclusion in seismic design codes. Soil Dynamics and Earthquake Engineering 2018;104:88–105. https://doi.org/10.1016/j.soildyn.2017.09.023.
[31] Chioccarelli E, Iervolino I. Sensitivity analysis of directivity effects on PSHA. BGTA 2013. https://doi.org/10.4430/bgta0099.
[32] Chioccarelli E, Iervolino I. Near-source seismic hazard and design scenarios: NEAR-SOURCE SEISMIC HAZARD AND DESIGN SCENARIOS. Earthquake Engng Struct Dyn 2013;42:603–22. https://doi.org/10.1002/eqe.2232.
[33] Burks LS, Baker JW. A predictive model for fling-step in near-fault ground motions based on recordings and simulations. Soil Dynamics and Earthquake Engineering 2016;80:119–26. https://doi.org/10.1016/j.soildyn.2015.10.010.
[34] Burks LS. Ground motion simulations: Validation and application for civil engineering problems. Stanford University; 2014.
[35] Abrahamson NA. Velocity pulses in near-fault ground motions. Proceedings of the UC Berkeley—CUREE Symposium in Honor of Ray Clough and Joseph Penzien: Berkeley, California, 2002, p. 40–1.
[36] Kamai R, Abrahamson N, Graves R. Adding fling effects to processed ground-motion time histories. Bulletin of the Seismological Society of America 2014;104:1914–29.
[37] Bray JD, Rodriguez-Marek A. Characterization of forward-directivity ground motions in the near-fault region. Soil Dynamics and Earthquake Engineering 2004;24:815–28.
[38] Pacor F, Felicetta C, Lanzano G, Sgobba S, Puglia R, D'Amico M, et al. NESS1: A worldwide collection of strong-motion data to investigate near-source effects. Seismological Research Letters 2018;89:2299–313.
[39] Hall JF, Heaton TH, Halling MW, Wald DJ. Near-Source Ground Motion and its Effects on Flexible Buildings. Earthquake Spectra 1995;11:569–605.
[40] Jamnani HH, Karbassi A, Lestuzzi P. Fling-step effect on the seismic behaviour of high-rise RC buildings during the Christchurch earthquake. 2013 NZSEE Conference, 2013.
[41] Ventura CE, Archila M, Bebamzadeh A, Liam Finn WD. Large coseismic displacements and tall buildings. The Structural Design of Tall and Special Buildings 2011;20:85–99.
[42] Sehhati R, Rodriguez-Marek A, ElGawady M, Cofer WF. Effects of near-fault ground motions and equivalent pulses on multi-story structures. Engineering Structures 2011;33:767–79.
[43] Champion C, Liel A. The effect of near-fault directivity on building seismic collapse risk. Earthquake Engineering & Structural Dynamics 2012;41:1391–409. https://doi.org/10.1002/eqe.1188.
[44] Medina RA, Krawinkler H. Influence of hysteretic behavior on the nonlinear response of frame structures. 13th World Conference on Earthquake Engineering, 2004.
[45] Motazedian D, Atkinson GM. Stochastic finite-fault modeling based on a dynamic corner frequency. Bulletin of the Seismological Society of America 2005;95:995–1010.
[46] Boore DM. Simulation of ground motion using the stochastic method. Pure and Applied Geophysics 2003;160:635–76.
[47] Boore DM. Comparing stochastic point-source and finite-source ground-motion simulations: SMSIM and EXSIM. Bulletin of the Seismological Society of America 2009;99:3202–16.
[48] Alterman Z, Karal Jr FC. Propagation of elastic waves in layered media by finite difference methods. Bulletin of the Seismological Society of America 1968;58:367–98.
[49] Galvez P, Ampuero J-P, Dalguer LA, Somala SN, Nissen-Meyer T. Dynamic earthquake rupture modelled with an unstructured 3-D spectral element method applied to the 2011 M 9 Tohoku earthquake. Geophysical Journal International 2014;198:1222–40.
[50] Smith WD. The application of finite element analysis to body wave propagation problems. Geophysical Journal International 1975;42:747–68.
[51] Taborda R, Roten D. Physics-based ground-motion simulation. Encyclopedia of Earthquake Engineering, Springer, Berlin, Heidelberg 2015:1–33.
[52] Frankel A, Vidale J. A three-dimensional simulation of seismic waves in the Santa Clara Valley, California, from a Loma Prieta aftershock. Bulletin of the Seismological Society of America 1992;82:2045–74.
[53] Shi Z, Day SM. Rupture dynamics and ground motion from 3-D rough-fault simulations. Journal of Geophysical Research: Solid Earth 2013;118:1122–41.
[54] Taborda R, Bielak J. Ground-motion simulation and validation of the 2008 Chino Hills, California, earthquake. Bulletin of the Seismological Society of America 2013;103:131–56.
[55] Graves R, Pitarka A. Refinements to the Graves and Pitarka (2010) broadband ground-motion simulation method. Seismological Research Letters 2015;86:75–80.

[56] Graves RW, Pitarka A. Broadband Ground-Motion Simulation Using a Hybrid ApproachBroadband Ground-Motion Simulation Using a Hybrid Approach. Bulletin of the Seismological Society of America 2010;100:2095–123. https://doi.org/10.1785/0120100057.
[57] Tinti E, Fukuyama E, Piatanesi A, Cocco M. A kinematic source-time function compatible with earthquake dynamics. Bulletin of the Seismological Society of America 2005;95:1211–23.
[58] Ida Y. Stress concentration and unsteady propagation of longitudinal shear cracks. Journal of Geophysical Research 1973;78:3418–29.
[59] Palmer AC, Rice JR. The growth of slip surfaces in the progressive failure of over-consolidated clay. Proceedings of the Royal Society of London A Mathematical and Physical Sciences 1973;332:527–48.
[60] Andrews DJ. Rupture velocity of plane strain shear cracks. Journal of Geophysical Research 1976;81:5679–87.
[61] Dieterich JH. Modeling of rock friction: 1. Experimental results and constitutive equations. Journal of Geophysical Research: Solid Earth 1979;84:2161–8.
[62] Ruina A. Slip instability and state variable friction laws. Journal of Geophysical Research: Solid Earth 1983;88:10359–70.
[63] Dascalu C, Ionescu IR, Campillo M. Fault finiteness and initiation of dynamic shear instability. Earth and Planetary Science Letters 2000;177:163–76. https://doi.org/10.1016/S0012-821X(00)00055-8.
[64] Freund LB. Dynamic fracture mechanics. Cambridge university press; 1998.
[65] Day SM, Dalguer LA, Lapusta N, Liu Y. Comparison of finite difference and boundary integral solutions to three-dimensional spontaneous rupture. Journal of Geophysical Research: Solid Earth 2005;110.
[66] Harris RA, Barall M, Archuleta R, Dunham E, Aagaard B, Ampuero JP, et al. The SCEC/USGS dynamic earthquake rupture code verification exercise. Seismological Research Letters 2009;80:119–26.
[67] Harris RA, Barall M, Aagaard B, Ma S, Roten D, Olsen K, et al. A suite of exercises for verifying dynamic earthquake rupture codes. Seismological Research Letters 2018;89:1146–62. https://doi.org/10.1785/0220170222.
[68] Dabaghi M, Almikati A. simulation of near-field ground motions for specified earthquake source and site characteristics. 5th International Symposium on the Effects of Surface Geology, Taipei, Taiwan: 2015.
[69] Chioccarelli E, Iervolino I. Near-source seismic hazard and design scenarios. Earthquake Engineering & Structural Dynamics 2013;42:603–22.
[70] Pacor F, Gallovič F, Puglia R, Luzi L, D'Amico M. Diminishing high-frequency directivity due to a source effect: Empirical evidence from small earthquakes in the Abruzzo region, Italy. Geophys Res Lett 2016;43:5000–8. https://doi.org/10.1002/2016GL068546.
[71] Ben-Menahem A. Radiation of seismic surface-waves from finite moving sources. Bulletin of the Seismological Society of America 1961;51:401–35.
[72] Akkar SD, Miranda E. Statistical Evaluation of Approximate Methods for Estimating Maximum Deformation Demands on Existing Structures. J Struct Eng 2005;131:160–72. https://doi.org/10.1061/(ASCE)0733-9445(2005)131:1(160).
[73] Yi W-J, Zhang H-Y, Kunnath SK. Probabilistic Constant-Strength Ductility Demand Spectra. J Struct Eng 2007;133:567–75. https://doi.org/10.1061/(ASCE)0733-9445(2007)133:4(567).
[74] Farrow KT, Kurama YC. SDOF displacement ductility demands based on smooth ground motion response spectra. Engineering Structures 2004;26:1713–33. https://doi.org/10.1016/j.engstruct.2004.06.003.
[75] International Code Council (ICC). International Building Code. International Code Council, Falls Church, VA 2000.
[76] Lingfeng K, Maosheng G, Zhanxuan Z. The effect of duration of strong ground motion on the ductility demand of SDOF structure. IOP Conf Ser: Earth Environ Sci 2019;304:032079. https://doi.org/10.1088/1755-1315/304/3/032079.
[77] Hatzigeorgiou GD. Ductility demand spectra for multiple near- and far-fault earthquakes. Soil Dynamics and Earthquake Engineering 2010;30:170–83. https://doi.org/10.1016/j.soildyn.2009.10.003.
[78] Krawinkler H, Medina R, Alavi B. Seismic drift and ductility demands and their dependence on ground motions. Engineering Structures 2003;25:637–53. https://doi.org/10.1016/S0141-0296(02)00174-8.
[79] Bayless J. Bayless-Somerville directivity model. Chapter 3 of Pacific Earthquake Engineering Research Center Report PEER-2013 2013;9.
[80] Spudich P, Chiou BS. Directivity in NGA earthquake ground motions: Analysis using isochrone theory. Earthquake Spectra 2008;24:279–98.
[81] Naumoski N, Tso WK, Heidebrecht AC. A selection of representative strong ground motion earthquake records having different A/V ratios. Report No. EERG 88/01. Earthquake Engineering Research Group,

McMaster University, Hamilton, Ontario 1988.
[82] Dobry R, Idriss IM, Ng E. Duration characteristics of horizontal components of strong-motion earthquake records. Bulletin of the Seismological Society of America 1978;68:1487–520.
[83] Kramer SL. Geotechnical earthquake engineering. Pearson Education India; 1996.
[84] Arias A. Measure of Earthquake Intensity. Massachusetts Inst. of Tech., Cambridge. Univ. of Chile, Santiago de Chile; 1970.
[85] Reed JW, Anderson N, Chokshi NC, Kennedy RP, Metevia WJ, Ostrom DK, et al. A criterion for determining exceedance of the operating basis earthquake: Final report. Electric Power Research Inst.; 1988.
[86] Von Thun JL. Earthquake ground motions for design and analysis of dams. Earthquake Engineering and Soil Dynamics II-Recent Advances in Ground-Motion Evaluation 1988.
[87] Housner GW. Intensity of ground motion during strong earthquakes 1952.
[88] Maechling PJ, Silva F, Callaghan S, Jordan TH. SCEC broadband platform: System architecture and software implementation. Seismological Research Letters 2015;86:27–38.
[89] Paolucci R, Gatti F, Infantino M, Smerzini C, Özcebe AG, Stupazzini M. Broadband Ground Motions from 3D Physics-Based Numerical Simulations Using Artificial Neural NetworksBroadband Ground Motions from 3D PBSs Using ANNs. Bulletin of the Seismological Society of America 2018;108:1272–86.
[90] Withers, K. B., Olsen, K. B, Shi, Z., Day, S. M.,, Takedatsu, R. SSA 2013 Annual Meeting Announcement. Seismological Research Letters 2013;84:258–397. https://doi.org/10.1785/0220130011.

TABLES

Table 1. Simulation parameters adopted for dynamic rupture simulations

Parameter	Symbol	Value
Bulk Properties		
P wave speed	α	6 km/sec
S wave speed	β	3.46 km/sec
Density	ρ	2670 kg/m^3
Poisson's ratio	ν	0.25
Initial background shear stress	τ_0	70.0 MPa
Initial background normal stress (compression)	σ_0	120 MPa
Fault geometry and material property		
Length of fault	L	30 km
Width of fault	W	15 km
Spectral element size		400 m
Number of GLL nodes		5
Friction parameters in the rupture zone		
Slip weakening distance	D_c	0.4 m
Dynamic frictional stress	τ_d	63 MPa
Static frictional stress	τ_s	81.24 MPa

Nucleation parameters		
Nucleation patch size	square patch	3 km
Depth	d	1.5 km
Initial shear stress	τ_{nuc}	81.6 MPa

FIGURES

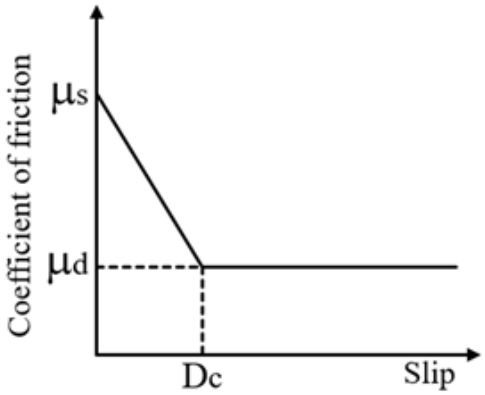

Figure 1: Slip weakening friction law. The ratio of initial shear traction to initial normal traction would somewhere be typically between μ_s and μ_d.

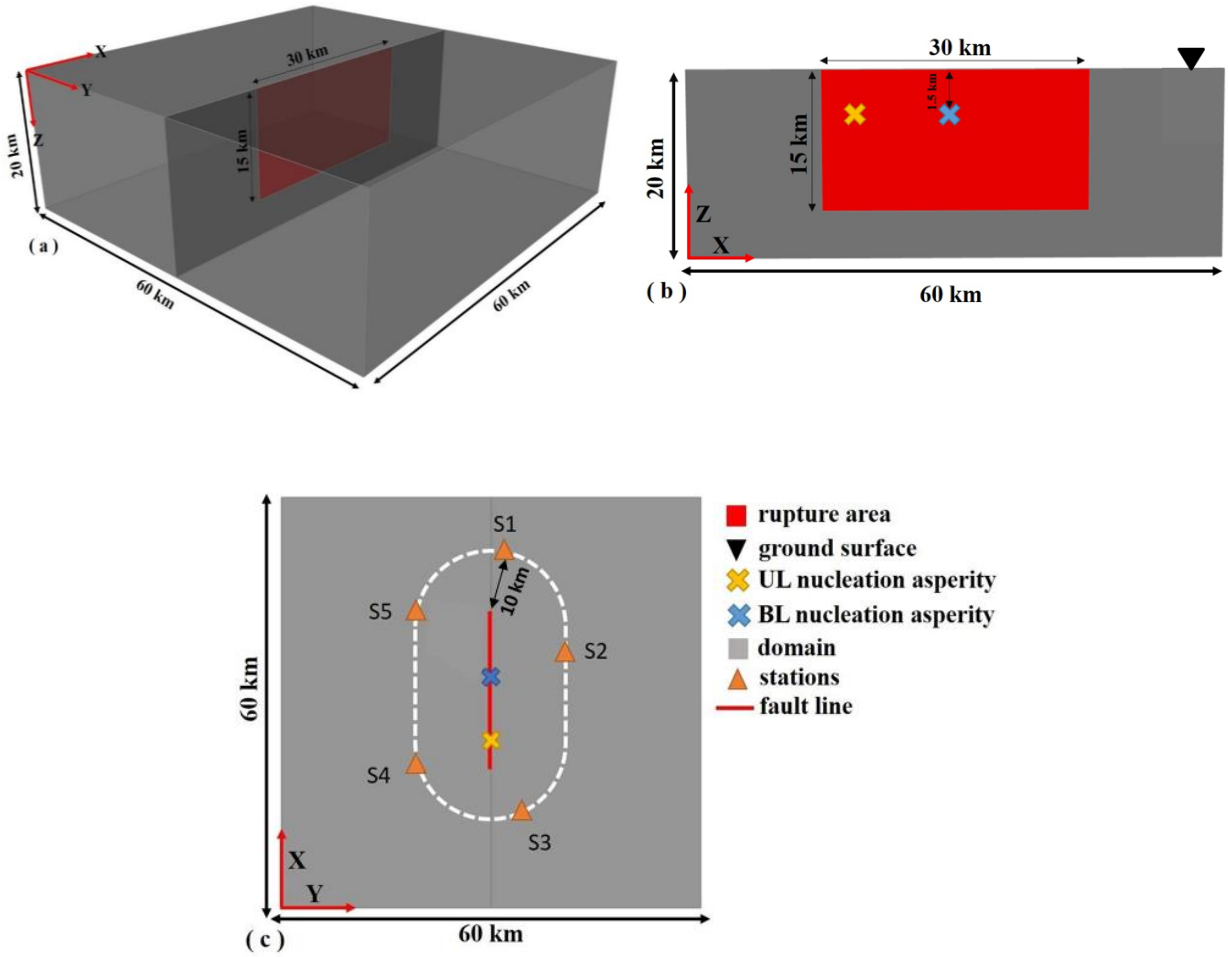

Figure 2: (a) A schematic diagram showing the positioning of a vertical strike-slip fault, (b) the fault section along with the nucleation patch for simulation of bilateral (BL) rupture (denoted by a blue cross) and unilateral (UL) rupture (denoted by a yellow cross), (c) the positioning and naming of stations with respect to the surface fault trace.

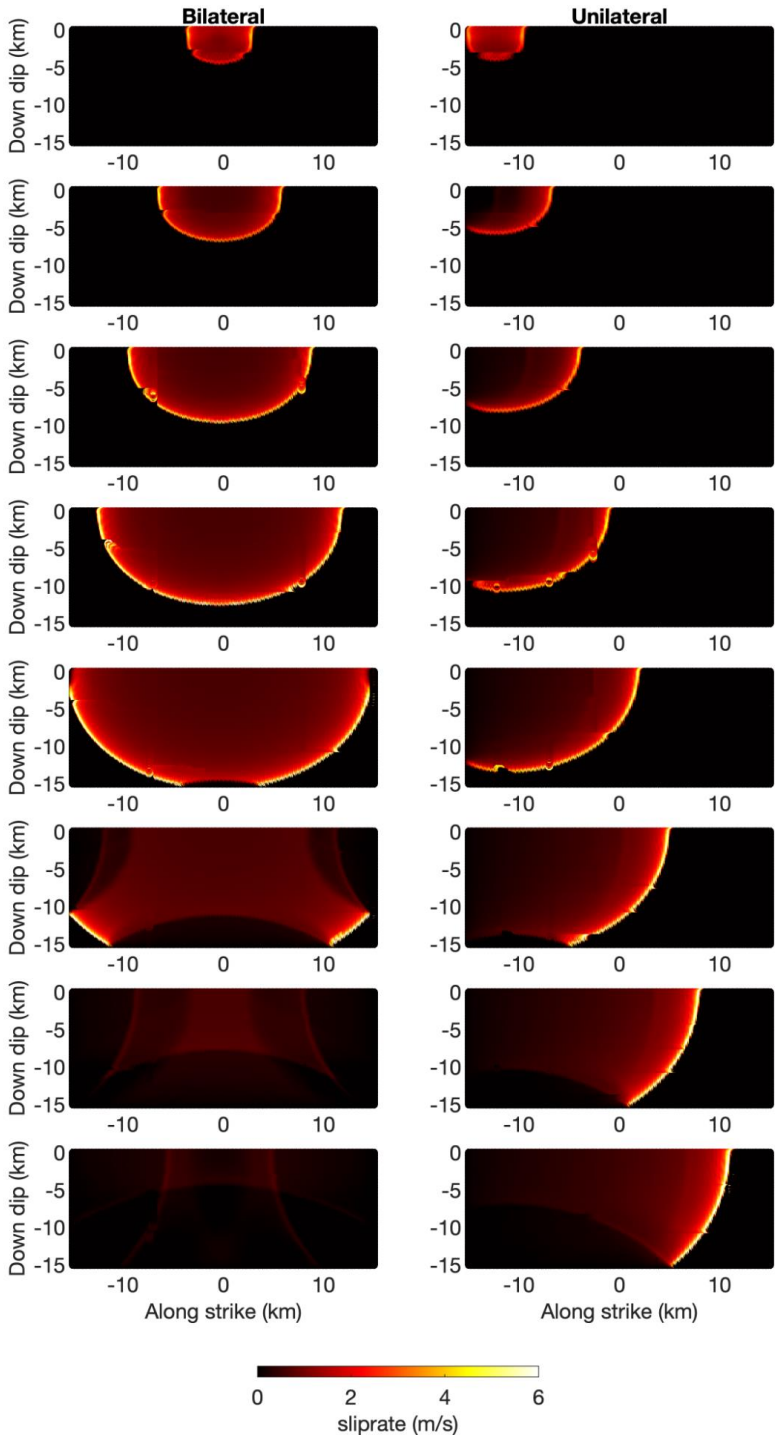

Figure 3: Evolution of slip rate on the fault plane for the two scenarios. Snapshots are shown every 1 sec apart.

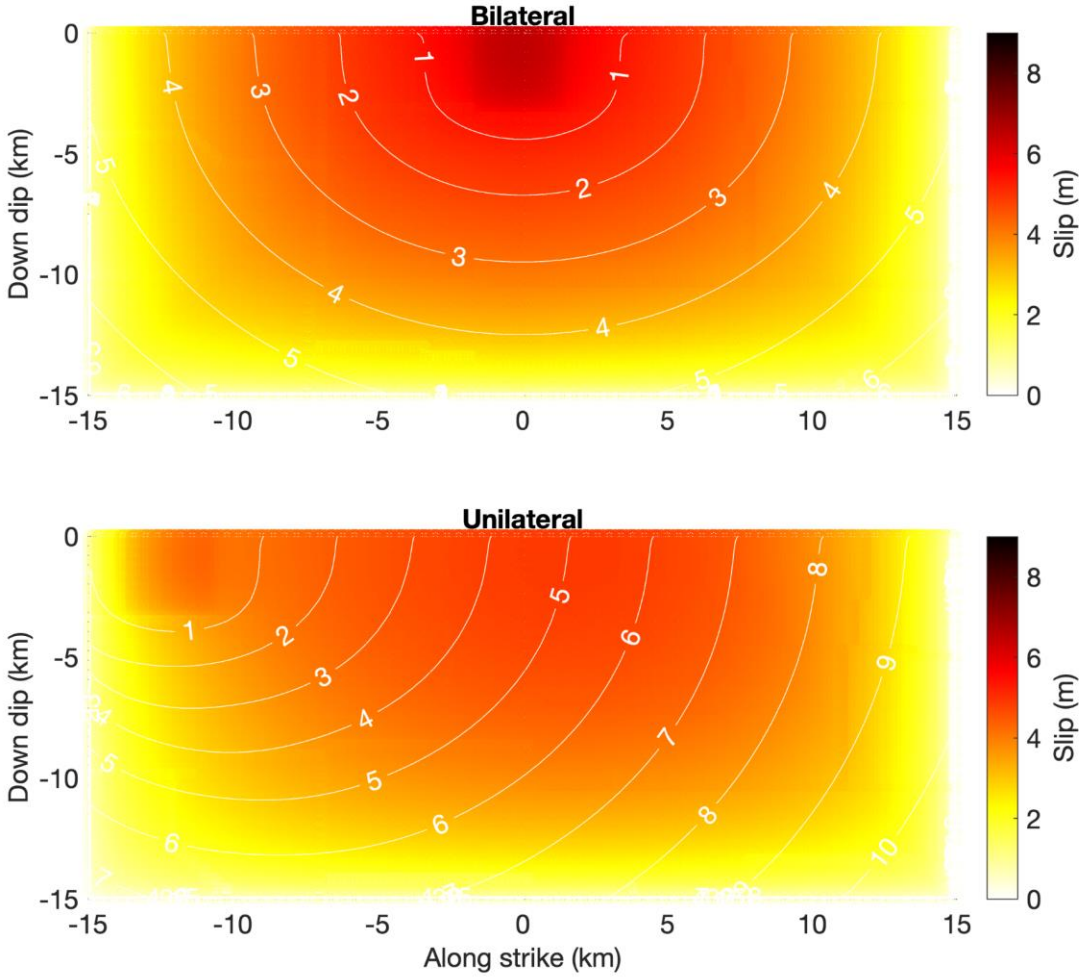

Figure 4: Final slip distribution along with the rupture contours on the fault plane for the two scenarios.

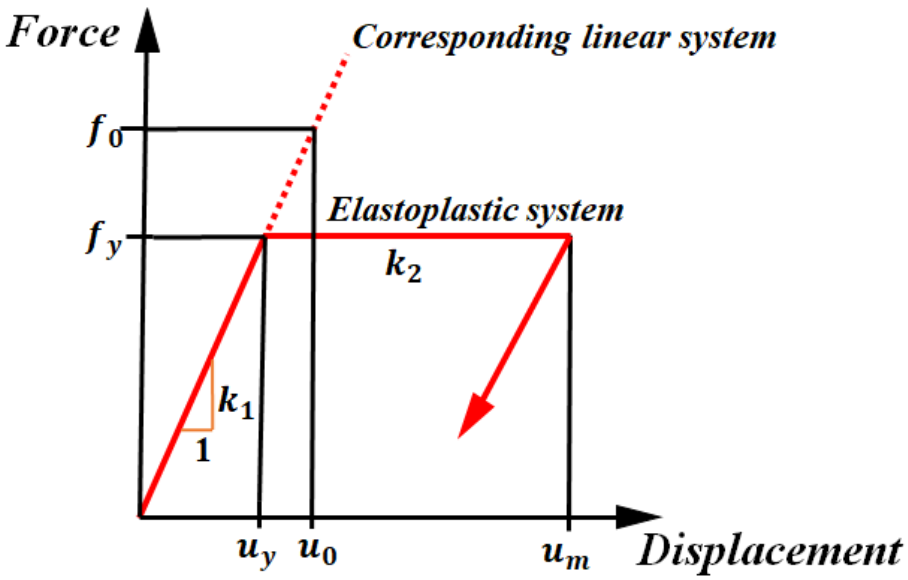

Figure 5: Load-deformation model of the bilinear inelastic SDoF system considered

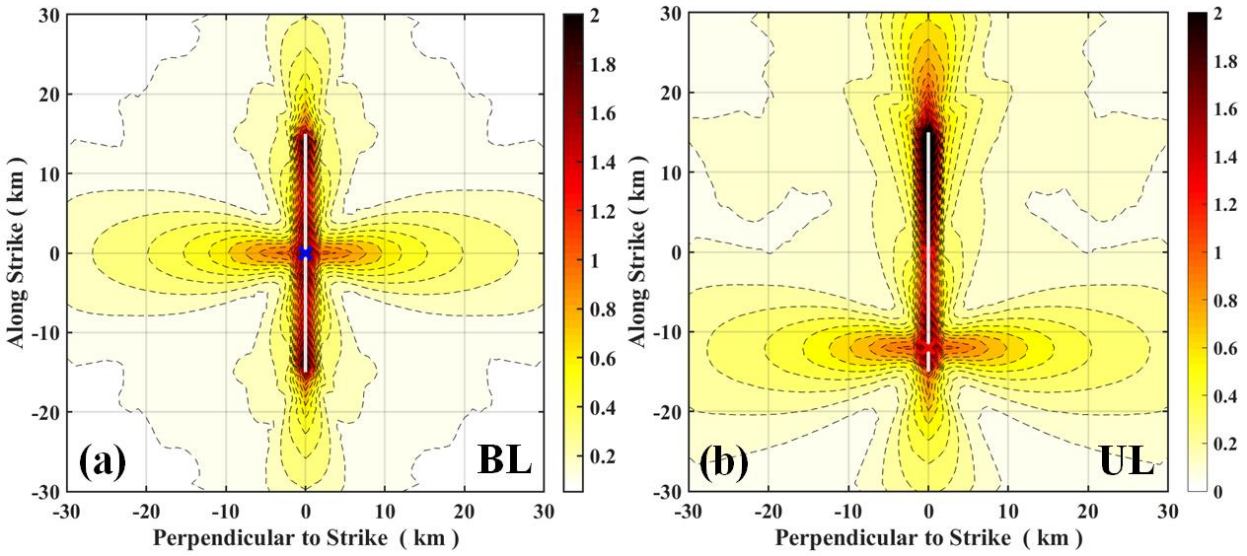

Figure 6: Map view of peak ground velocity (PGV [m/s]) contours for the two scenarios. (a) Bilateral (BL) rupture scenario (b) Unilateral (UL) rupture scenario.

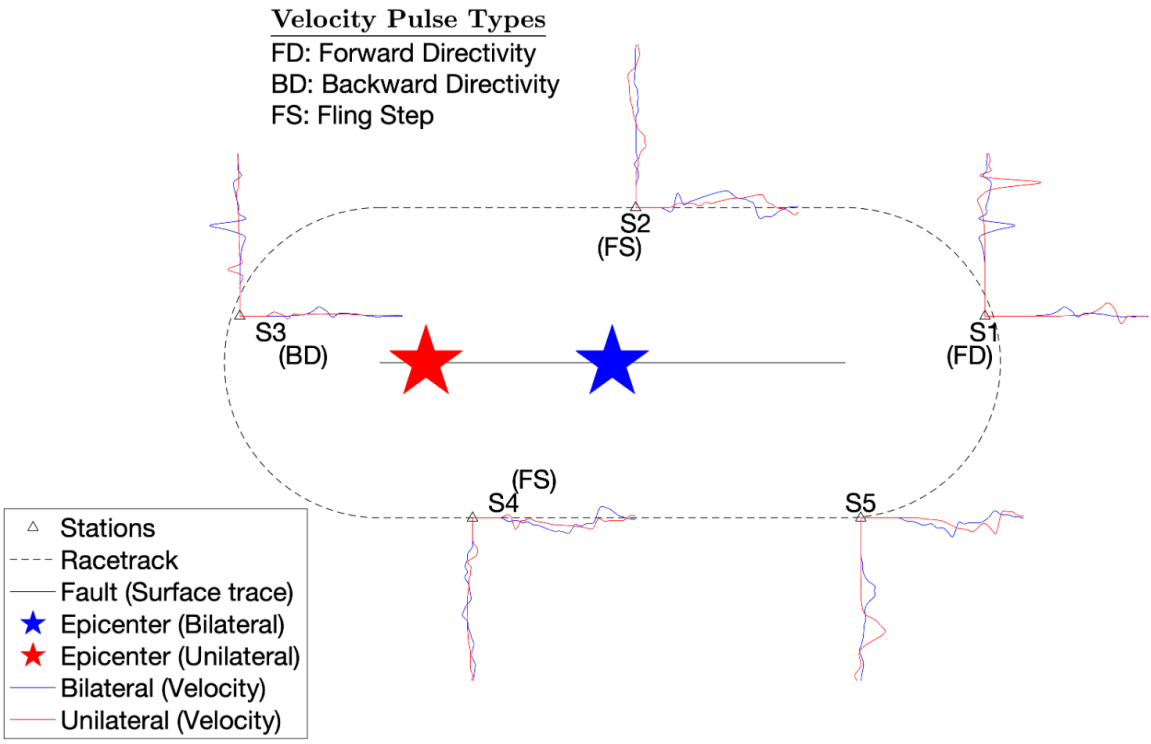

Figure 7: Velocity-time series of fault parallel (plotted horizontal) components and fault normal (plotted vertically) components. Data is low-pass filtered with a corner at 1 Hz.

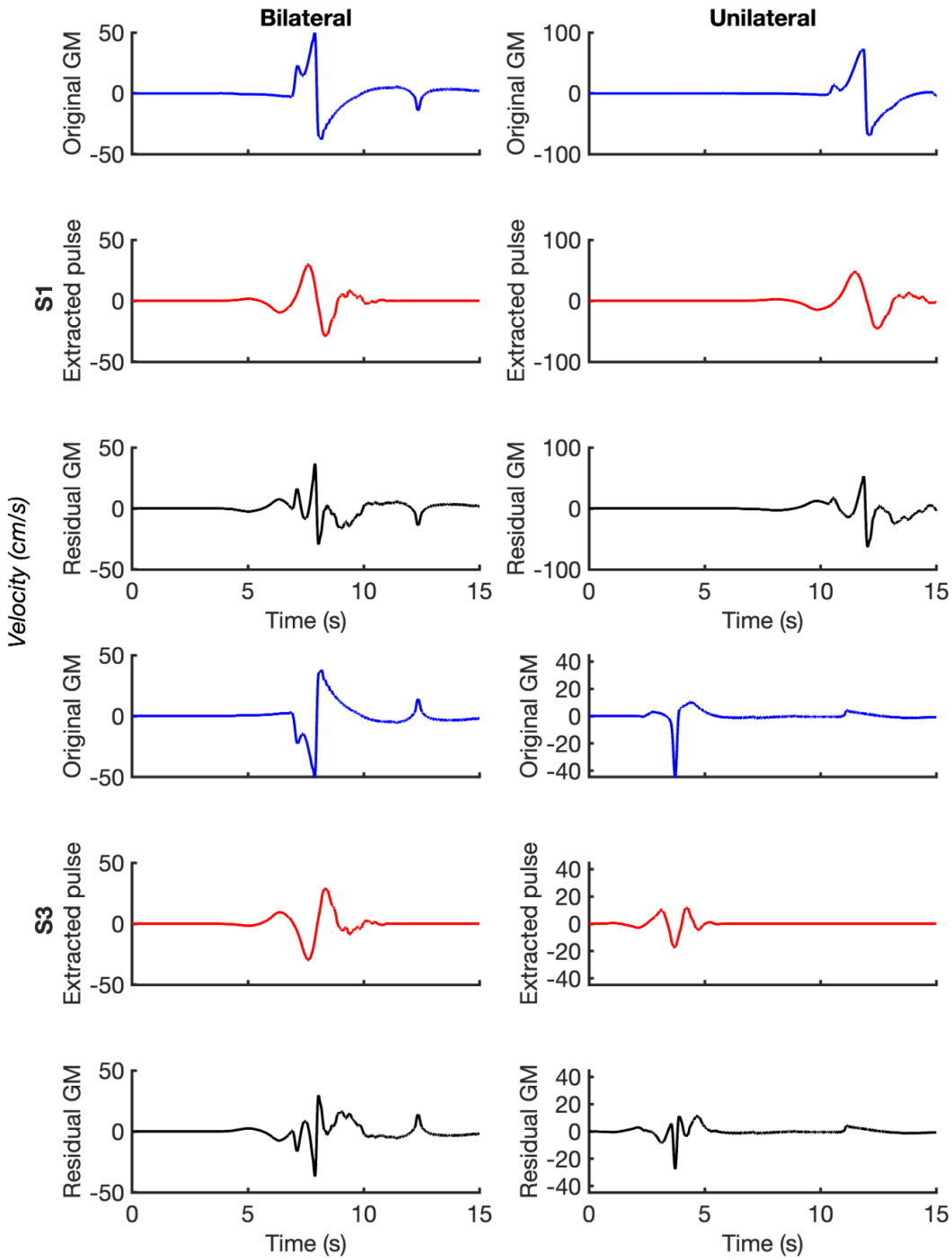

Figure 8: Pulse extraction using Baker's wavelet algorithm for the velocity ground motion (GM) of the forward-directivity (S1) and the backward-directivity (S3) stations, for the bilateral and unilateral cases.

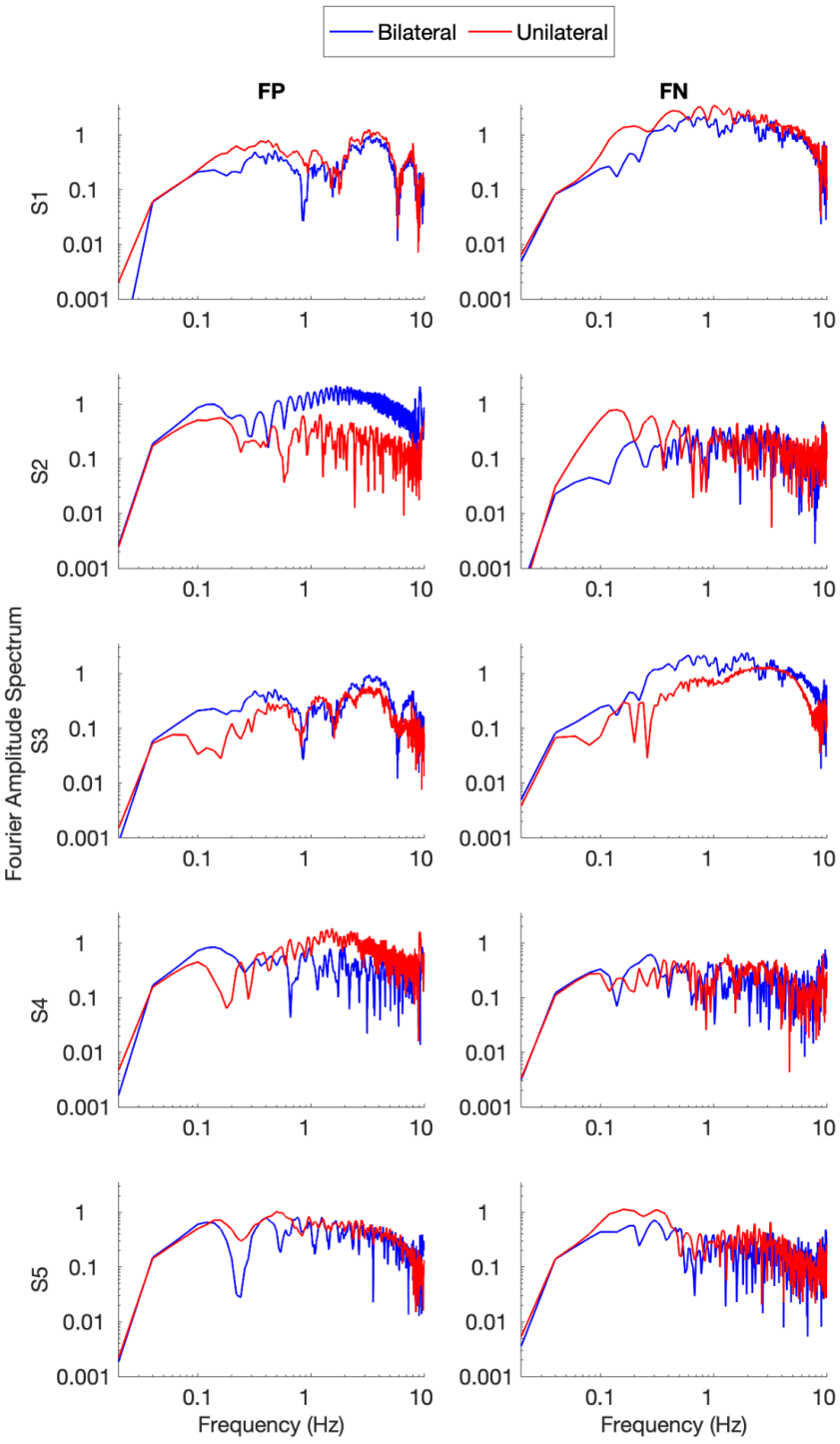

Figure 9: Fourier amplitude acceleration of the 5 racetrack stations FP component (left), FN component (right). Blue is bilateral and red is unilateral.

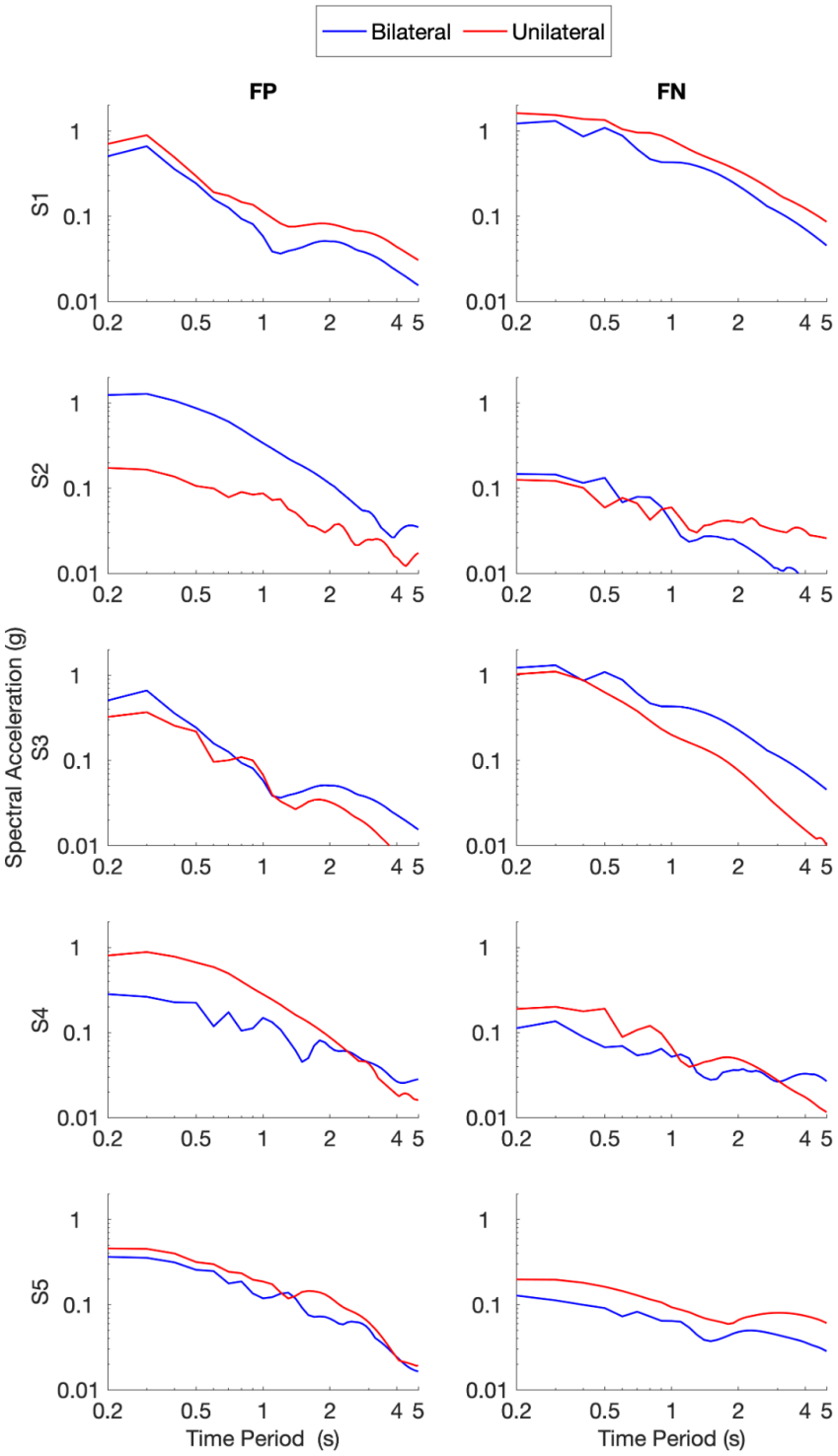

Figure 10: Spectral acceleration of the 5 racetrack stations FP component (left column), FN component (right column). Blue is bilateral and red is unilateral.

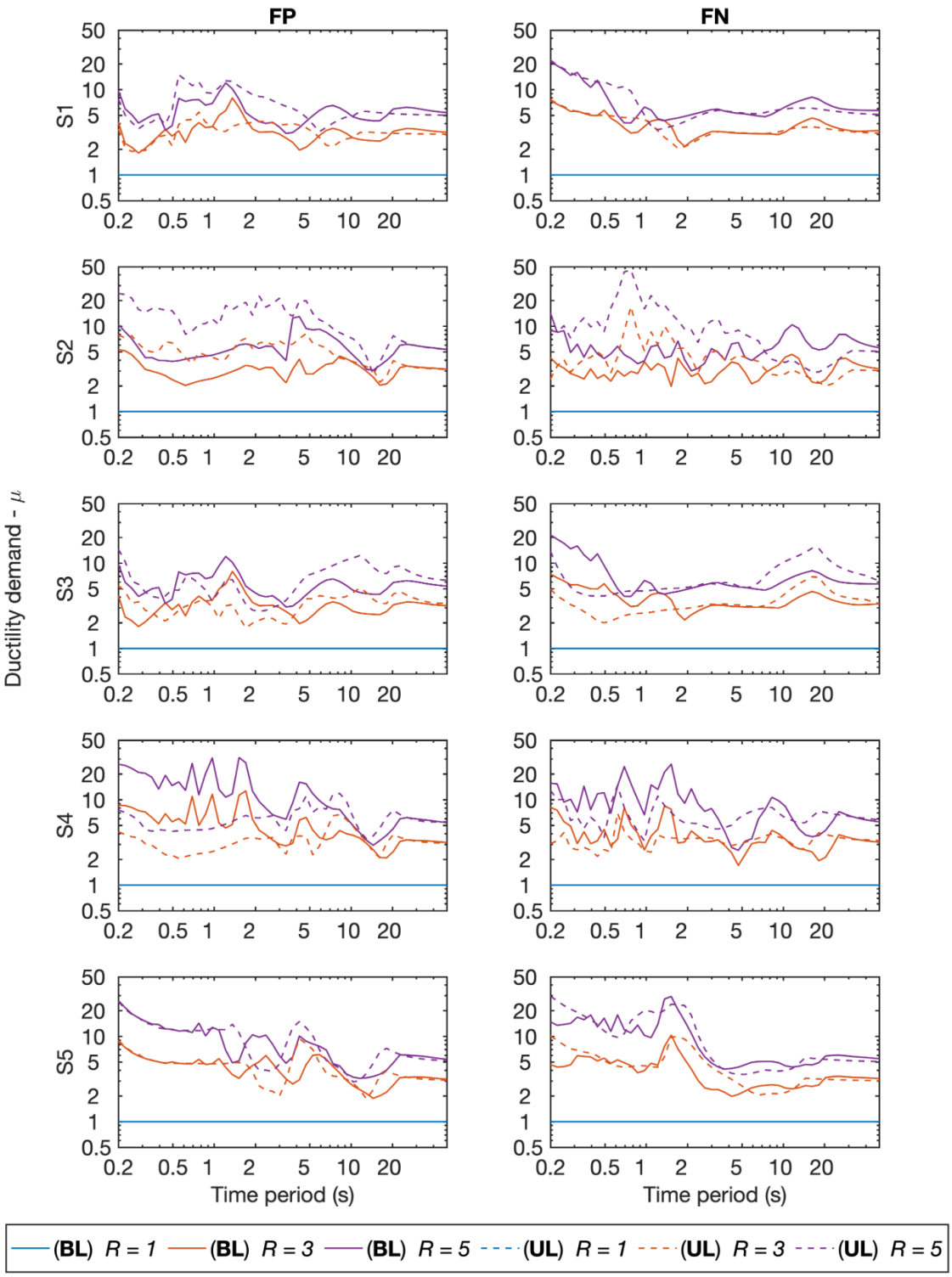

Figure 11: Ductility demand spectra for elastoplastic systems of the 5 racetrack stations FP component (left column), FN component (right column).

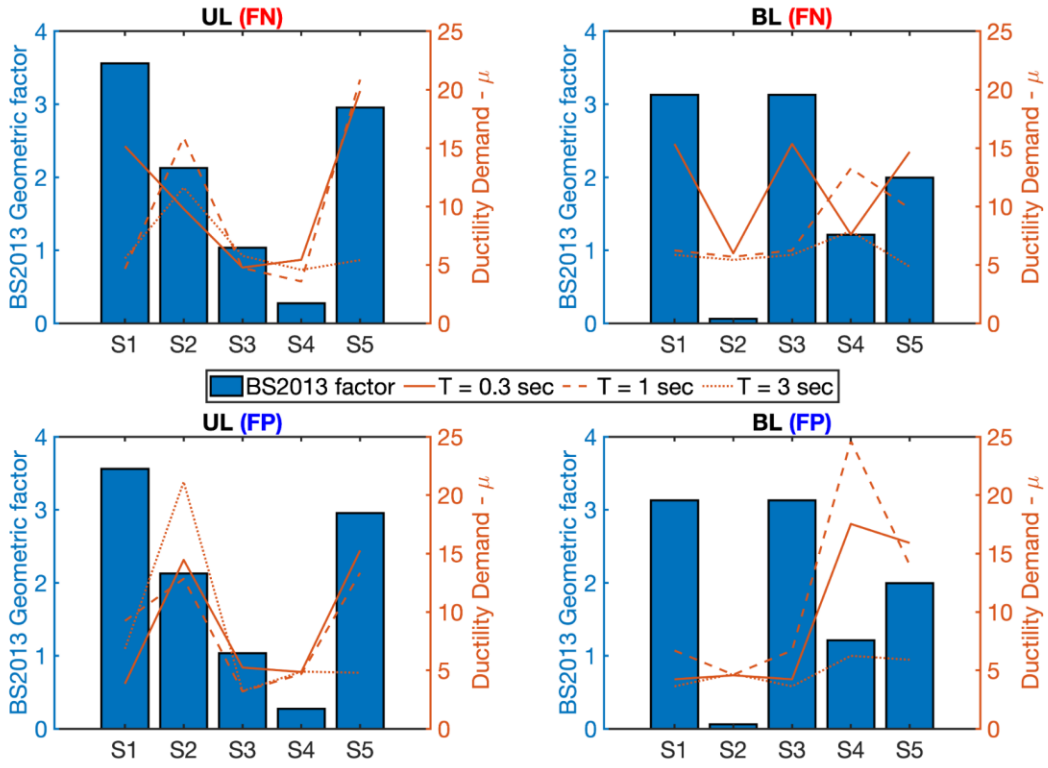

Figure 12: Correlations between Bayless and Somerville (2013) geometric factor ductility demand of inelastic SDOF systems with 3 natural periods (T = 0.3, 1, 3 sec) at the 5 stations for R = 5. UL and BL denote unilateral and bilateral ruptures. FN and FP denote fault-normal and fault-parallel components.

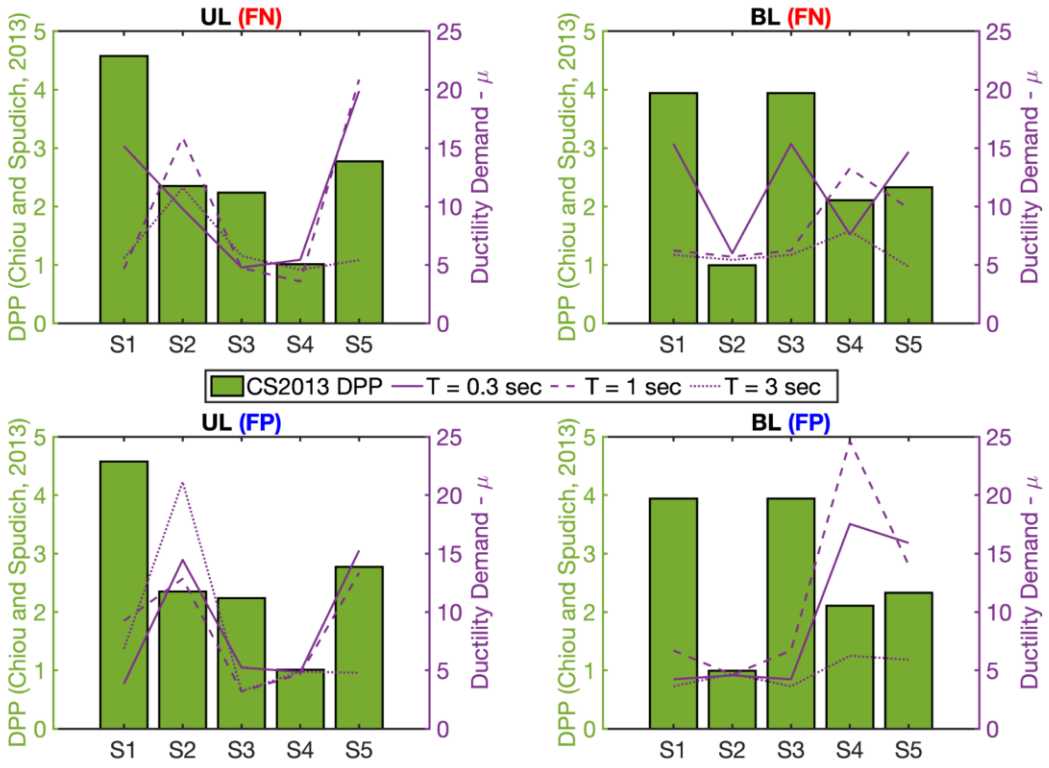

Figure 13: Correlations between Chiou and Spudich (2013) factor and ductility demand of inelastic SDOF systems with 3 natural periods (T = 0.3, 1, 3 sec) at the 5 stations for R = 5. UL and BL denote unilateral and bilateral ruptures. FN and FP denote fault-normal and fault-parallel components.

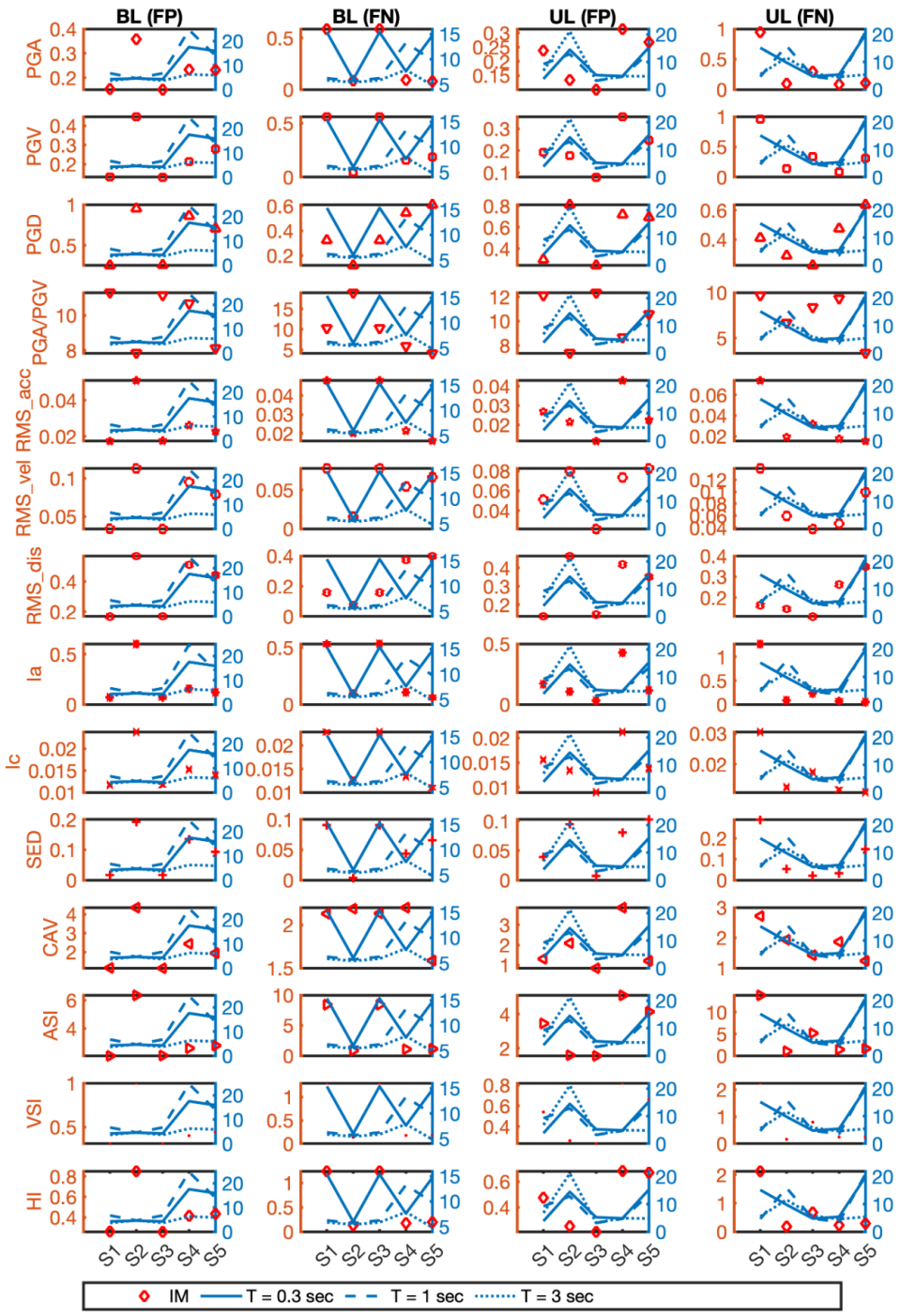

Figure 14: Correlations between ground motion intensity measurements with ductility demand for the inelastic SDOF systems with 3 natural periods (T = 0.3, 1, 3 sec) at the 5 racetrack stations for R = 5.